

Microinstabilities at perpendicular collisionless shocks: A comparison of full particle simulations with different ion to electron mass ratio

Takayuki Umeda* and Yoshitaka Kidani

Solar-Terrestrial Environment Laboratory, Nagoya University, Nagoya 464-8601, JAPAN

Shuichi Matsukiyo†

Earth System Science and Technology, Kyushu University, Kasuga 816-8580, JAPAN

Ryo Yamazaki‡

Department of Physics and Mathematics, Aoyama Gakuin University, Sagami-hara 252-5258, JAPAN

A full particle simulation study is carried out for studying microinstabilities generated at the shock front of perpendicular collisionless shocks. The structure and dynamics of shock waves are determined by Alfvén Mach number and plasma beta, while microinstabilities are controlled by the ratio of the upstream bulk velocity to the electron thermal velocity and the plasma-to-cyclotron frequency. Thus, growth rates of microinstabilities are changed by the ion-to-electron mass ratio, even with the same Mach number and plasma beta. The present two-dimensional simulations show that the electron cyclotron drift instability is dominant for a lower mass ratio, and electrostatic electron cyclotron harmonic waves are excited. For a higher mass ratio, the modified two-stream instability is dominant and oblique electromagnetic whistler waves are excited, which can affect the structure and dynamics of collisionless shocks by modifying shock magnetic fields.

PACS numbers: 52.35.Tc; 52.35.Qz; 52.65.-y; 52.65.Rr;

I. INTRODUCTION

Collisionless shocks have been investigated by full particle (Particle-In-Cell) simulations for more than four decades since early 1970's [1]. The full particle method handles both electron-scale microphysics and ion-scale shock non-stationarity simultaneously because both electrons and ions are treated as individual charged particles. However, a reduced ion-to-electron mass ratio (m_i/m_e) is commonly used in the full particle method to reduce the computational cost.

It is well known that structures and dynamics of shock waves are determined by the following two dimensionless parameters, i.e., Alfvén Mach number

$$M_A = \frac{u_1}{c} \frac{\omega_{pi1}}{\omega_{ci1}} = \frac{u_1}{c} \frac{\omega_{pe1}}{\omega_{ce1}} \sqrt{\frac{m_i}{m_e}}. \quad (1)$$

and the ratio of the thermal plasma pressure to the magnetic pressure (plasma beta)

$$\beta_e = \frac{2v_{te1}^2 \omega_{pe1}^2}{c^2 \omega_{ce1}^2}, \quad \beta_i = \frac{2v_{ti1}^2 \omega_{pi1}^2}{c^2 \omega_{ci1}^2}, \quad (2)$$

where c , u , ω_p , ω_c , v_t and m represent the speed of light, upstream bulk velocity, plasma frequency, cyclotron frequency, thermal velocity and mass, respectively, with the subscripts “ i ” and “ e ” being ion and electron, respectively. Here the subscript “1” denotes upstream.

It is well known that a part of incoming ions are reflected at the shock front of perpendicular and quasi-perpendicular shocks. The reflection of ions results in the deceleration of incoming electrons so that the conservation of the total current (the zero current condition in the shock normal direction) is satisfied. Consequently, a relative bulk velocity between the incoming electrons and the incoming/reflected ions arises. Previous self-consistent kinetic simulation studies revealed that there exist various types of microinstabilities at the shock front of perpendicular and quasi-perpendicular shocks in which reflected ions play essential roles in dissipative processes. The free energy source of these microinstabilities is the relative drift (current) between incoming electrons and incoming/reflected ions.

The ratio of the relative drift velocity to the electron thermal velocity is important for controlling the type of microinstabilities (or the effect of electron thermal damping to waves). This ratio is proportional to the ratio of the upstream bulk velocity to the electron thermal velocity. From the equations of Alfvén Mach number and electron beta, we obtain

$$\frac{u_1}{v_{te1}} = M_A \frac{\sqrt{2}}{\sqrt{\beta_e}} \sqrt{\frac{m_e}{m_i}}. \quad (3)$$

This relation means that the ratio of the upstream bulk velocity to the electron thermal velocity becomes larger with larger Alfvén Mach number, smaller electron beta, or smaller mass ratio. Note that the actual amount of free energy relative to the electron thermal energy ($m_i u_{x1}^2 / m_e v_{te1}^2$) is independent of the mass ratio.

If the relative velocity between electrons and ions exceeds the electron thermal velocity, electrostatic waves

*Email: umeda@stelab.nagoya-u.ac.jp

†Email: matsukiyo@esst.kyushu-u.ac.jp

‡Email: ryo@phys.aoyama.ac.jp

are excited by current-driven instabilities such as the Buneman-type instability (BI) [2] or the electron cyclotron drift instability (ECDI) [3, 4]. At high-Mach-number perpendicular shocks, the relative velocity between incoming electrons and reflected ions commonly becomes much faster than the electron thermal velocity. Then, the BI becomes dominant, and electrostatic waves are excited at the upper hybrid resonance frequency [5]. At lower-Mach-number ($M_A < 10$) perpendicular shocks, the relative velocity between incoming electrons and incoming/reflected ions becomes close to the electron thermal velocity. Then, the growth rate of the BI becomes small because of damping by thermal electrons, and the ECDI becomes dominant, which excites electrostatic waves at multiple electron cyclotron harmonic frequencies [6]. When the relative velocity between incoming electrons and incoming/reflected ions becomes slower than the electron thermal velocity at lower-Mach-number perpendicular shocks, high-frequency electrostatic waves are not excited due to damping by thermal electrons, and the modified two-stream instability (MTSI) becomes dominant [7, 8, 9, 10, 11]. Then, obliquely propagating electromagnetic whistler mode waves are excited at a frequency between the electron cyclotron frequency and the lower hybrid resonance frequency [12, 13, 14, 15, 16, 17, 18].

The previous theoretical work has shown that the growth rate of the MTSI is strongly affected by the ion-to-electron mass ratio (m_i/m_e), but not by the ratio of the electron plasma to cyclotron frequency (ω_{pe}/ω_{ce}) [14]. It has also been confirmed by the previous one-dimensional (1D) full particle simulation studies that the mass ratio affects the shock dynamics as well as the microinstability [13, 15]. In the present study, we vary the mass ratio and frequency ratio as shown in Table I. Even when the Alfvén Mach number and the electron beta are fixed, the ratio of the plasma frequency to cyclotron frequency (ω_p/ω_c) can take an arbitrary value, because c/v_{te} or u_1/c can also take arbitrary values. The frequency ratio may also control the type of microinstabilities by determining the linear dispersion relation of background plasma. It should be noted that the effect of the frequency ratio is not included in hybrid simulations where ions are treated as particles while electrons are treated as a (massless) fluid. That is, the ion inertial length (c/ω_{pi}) and the ion gyro radii (v_{ti}/ω_{ci} and u_1/ω_{ci}) are defined but $\omega_{pi}/\omega_{ci} \rightarrow \infty$ and $c/v_{ti} \rightarrow \infty$ are assumed in hybrid simulations. Thus the full particle simulation is the unique approach to study the effect of both mass ratio and frequency ratio.

In the present study, we perform a series of two-dimensional (2D) full particle simulations of a perpendicular (the shock normal angle $\theta_{B_n} = 90^\circ$) collisionless shock with a low Mach number ($M_A = 6$) and a moderate beta ($\beta_i = \beta_e = 0.32$). We examine the impact of the mass ratio on microinstabilities at the shock front by fixing either $\omega_{pi1}/\omega_{ci1}$ or $\omega_{pe1}/\omega_{ce1}$ as shown in Table I.

II. SIMULATION SETUP

We use a 2D electromagnetic full particle code in which the full set of Maxwell's equations and the relativistic equation of motion for individual electrons and ions are solved in a self-consistent manner. The continuity equation for charge is also solved to compute the exact current density given by the motion of charged particles [19]. In the present simulation, the simulation domain is taken in the shock-rest frame [20, 21, 22]. The shock-rest-frame model is achieved by using the “relaxation method” [6, 23, 24], in which a collisionless shock is excited by an interaction between a supersonic plasma flow and a subsonic plasma flow moving in the same direction.

The initial state consists of two uniform regions separated by a discontinuity. In the upstream region that is taken in the left-hand side of the simulation domain, electrons and ions are distributed uniformly in space and are given random velocities (v_x, v_y, v_z) to approximate shifted Maxwellian momentum distributions with the drift velocity \vec{u}_1 , number density $n_1 \equiv \epsilon_0 m_e \omega_{pe1}^2 / e^2$, isotropic temperatures $T_{e1} \equiv m_e v_{te1}^2$ and $T_{i1} \equiv m_i v_{ti1}^2$, where e is the charge. Here, the subscripts “1” and “2” denote “upstream” and “downstream”, respectively. The upstream magnetic field \vec{B}_{01} with a magnitude of $m_e \omega_{ce1} / e$ is also assumed to be uniform. The downstream region taken in the right-hand side of the simulation domain is prepared similarly with the drift velocity \vec{u}_2 , density n_2 , isotropic temperatures T_{e2} and T_{i2} , and magnetic field \vec{B}_{02} .

We take the simulation domain in the x - y plane and assume an in-plane shock magnetic field (B_{y0}). The shock-normal magnetic field B_{x0} is set to be zero. That is, the shock-normal angle θ_{B_n} , which is defined as the angle between upstream magnetic field and shock-normal direction, is set as 90° in the present study. As a motional electric field, a uniform external electric field $E_{z0} = u_{x1} B_{y01} = u_{x2} B_{y02}$ is applied in both upstream and downstream regions, so that both electrons and ions drift along the x axis. At the left boundary of the simulation domain in the x direction, we inject plasmas with the same quantities as those in the upstream region, while plasmas with the same quantities as those in the downstream region are also injected from the right boundary in the x direction. We use absorbing boundaries to suppress non-physical reflection of electromagnetic waves at both ends of the simulation domain in the x direction [25], while the periodic boundaries are imposed in the y direction.

In the relaxation method, the initial condition is given by solving the shock jump conditions (Rankine-Hugoniot conditions) for a magnetized two-fluid isotropic plasma consisting of electrons and ions [26]. In order to determine a unique initial downstream state, we need given upstream quantities u_{x1} , ω_{pe1} , ω_{ce1} , v_{te1} , v_{ti1} and T_{i2}/T_{e2} .

In the present study, we fix the Mach number and plasma beta to $M_A = 6$ and $\beta_e = \beta_i = 0.32$. As shown in

TABLE I: Parameters for different simulation runs.

Run	m_i/m_e	$\omega_{pe1}/\omega_{ce1}$	$\omega_{pi1}/\omega_{ci1}$	u_{x1}/v_{te1}	c/v_{te1}	l_{i1}/λ_{De1}
A ^a	625	4.0	100.0	0.6	10.0	250
B	256	4.0	64.0	0.9375	10.0	160
C	100	4.0	40.0	1.5	10.0	100
D	25	4.0	20.0	3.0	10.0	50
E	256	6.25	100.0	0.9375	15.625	250
F	100	10.0	100.0	1.5	25.0	250
G	25	20.0	100.0	3.0	50.0	250

^a Umeda *et al.* [18]

Table I, we perform 7 different runs by varying the mass ratio (m_i/m_e) and frequency ratio. We fix ω_{pe}/ω_{ce} in Runs B-D. Then, the electron parameters are fixed while the ion parameters are changed. On the other hand, we fix ω_{pi}/ω_{ci} in Runs E-G. Then, the ion parameters are fixed while the electron parameters are changed.

The size of the simulation domain is $L_x = 32l_{i1}$ and $L_y = l_{i1}$ in the shock-normal and shock-tangential directions, respectively, where $l_{i1} = c/\omega_{pi1}$ is the ion inertial length. The grid spacing is set to be $\Delta x = \Delta y = \lambda_{De1}$ where λ_{De1} is the electron Debye length upstream. On the other hand, the time step is set to be $c\Delta t/\Delta x = 0.5$. These mean that the computational resource (the size of the simulation domain and the number of time step) increases with the mass ratio when the electron parameters are fixed (Runs A-D), while the computational resource becomes constant when the ion parameters are fixed (Runs E-G and A). We used 16 pairs of electrons and ions per cell in the upstream region and 64 pairs of electrons and ions per cell in the downstream region, respectively, at the initial state.

III. RESULTS

A. Simulation Results

Figure 1 shows the evolution of the perpendicular shock in Runs A-G. The snapshots of the magnetic field B_x , B_y , B_z components, the electric field E_x component, and the corresponding $x - v_x$ phase-space distribution function of ions at $\omega_{ci1}t = 10.2$ in Runs A-G are plotted in Figures A-G, respectively. The position is normalized by the ion inertial length $l_{i1} = c/\omega_{pi1}$. The magnitudes of magnetic field and electric field are normalized by the initial upstream magnetic field B_{y01} and the motional electric field E_{z0} , respectively. In the panel (a'), the tangential component of the magnetic field B_y in Run A is plotted as a function of position x and time t . Note that the tangential component of the magnetic field B_y in Runs B-G shows almost the same evolution as the panel (a').

In the present shock-rest-frame model, a shock wave is excited by the relaxation of the two plasmas with different quantities. Since the initial state is given by the shock jump conditions for a “two-fluid” plasma consist-

ing of electrons and ions, the kinetic effect is excluded in the initial state. Thus the excited shock slightly moves upstream. The shock front appears and disappears on a timescale of the ion cyclotron period in Figure 1a', which corresponds to the cyclic shock reformation [1, 27, 28].

In all the runs, a certain part of the incoming ions is reflected upstream at the shock ramp and the shock foot region is formed, which is called the broadening phase of the reformation. Consequently, microinstabilities are generated due to the relative drift between the reflected ions and the incoming electrons, and ion phase-space vortices in association with wave generation are formed as seen in the ion $x - v_x$ phase-space plots. The spatial size of the foot region corresponds to the gyro radius of reflected ions, which seems to be longer with respect to the ion inertial length as the mass ratio becomes smaller when the electron parameters are fixed (Runs A-D). It is found that the wavelength of the magnetic field B_z component in the shock normal direction becomes longer as the mass ratio becomes smaller. The excited waves in E_x and B_z components have the same wavelength in Runs A, B, C, E, and F, indicating the excitation of electromagnetic waves. Also, the wavelength is shorter with the fixed ω_{pi}/ω_{ci} than with the fixed ω_{pe}/ω_{ce} . However, the saturation amplitude of these waves is almost independent of the mass ratio (typically $\delta B_z^2 \sim 0.3B_0^2$). On the other hand, the excited waves in Runs D and G have a shorter wavelength in E_x component than in B_z component, indicating the excitation of electrostatic waves in the electric field E_x component. The typical timescale of the saturation of instabilities is $\sim 0.6/\omega_{ci1}$ from the beginning of the broadening phase (ion reflection). Note that the typical timescale of the reformation is $\sim 1.6/\omega_{ci1}$ in the present case.

In Figures 2 and 3, we show spectra of B_z and E_x components, respectively, for Runs A-G. These spectra are obtained by Fourier transformation in the range of $-6.5 \leq x/l_{i1} \leq -5.5$, $0 \leq y/l_{i1} \leq 1$, and $9.8 \leq \omega_{ci1}t \leq 10.6$. The intensity of B_z and E_x is normalized by B_{y01} and E_{z0} , respectively. In the top panels, the $\omega - k_x - k_y$ spectrum is reduced to the $k_x - k_y$ space by integrating over ω . In the bottom panels, the $\omega - k_x - k_y$ reduced to the $\omega - k_x$ space integrating over k_y .

The spectra of both B_z and E_x show that there are several wave modes. An ion-scale component exists at $\omega \sim 0$, $k_x \sim 0$ and $k_y \sim 0$, which may correspond to

L-mode ion-cyclotron waves due to the ion temperature anisotropy. However, this wave mode is not focused on in the present study because the present Fourier analysis cannot resolve ion scales.

In all the simulation runs, waves with an electron-scale wavelength are excited almost in the shock-normal direction ($k_y \sim 0$). The excited waves propagate mostly in both ($\pm x$) directions, but the waves propagate in the $-x$ direction are dominant. The phase velocity of the excited waves in the $-x$ direction estimated from the $\omega - k_x$ spectra corresponds to the drift velocity of the reflected ions. The phase velocity of the excited waves in the $+x$ direction corresponds to the drift velocity of the incoming ions.

In all the runs, the frequency of the B_z component is lower than the upstream electron cyclotron frequency ω_{ce1} but is higher than the upstream lower hybrid resonance frequency ($\omega_{LHR1}/\omega_{ce1} \sim 0.04$ in Run A, 0.06 in Runs B and E, 0.1 in Runs C and F, and 0.2 in Runs D and G). These properties agree well with the scenario that whistler mode waves propagating in the direction oblique to the upstream magnetic field are excited by the MTSI due to ion beams (incoming or reflected ions) across the shock magnetic field. In Runs D, F, and G, there are also enhancements of the E_x component at frequencies higher than the upstream electron cyclotron frequency ω_{ce1} but is lower than the upstream upper hybrid resonance frequency ($\omega_{UHR1}/\omega_{pe1} = 4.1$ in Run D, 10.0 in Run F, and 20.0 in Run G). These properties agree with the scenario that electron cyclotron harmonic waves propagating in the direction almost perpendicular to the upstream magnetic field excited by the ECDI due to ion beams (incoming or reflected ions) across the shock magnetic field. These results suggest that the ECDI is generated when the ion-to-electron mass ratio is relatively small.

B. Comparison with linear analysis

A previous linear analysis and numerical simulation by Matsukiyo and Scholer [16] suggested that there are two-types of instabilities due to both incoming and reflected ions. Hereafter, we refer to an instability due to incoming ions as “instability-1”, and refer to an instability due to reflected ions as “instability-2”.

In order to analyze the linear dispersion relation at the shock foot, we approximate the velocity distribution function with Maxwellian velocity distributions, that is given by

$$f(v) = \frac{n}{\sqrt{2\pi}V_t} \exp \left[-\frac{(v - V_d)^2}{2V_t^2} \right]. \quad (4)$$

For simplicity, we focus on the velocity distribution function only in the shock-normal direction (x component). The velocity distribution function $f(v_x)$ is modeled by the three-component plasma consisting of incoming ions (i1), reflected ions (i2) and bulk electrons (e). Figure 4

shows the typical velocity distribution functions of ions and electrons at the shock foot just before the generation of instabilities in Runs A-G. Table 2 shows detailed parameters for the Maxwellian velocity distribution functions estimated from Fig.4. The velocity, density and frequency are normalized by the upstream electron thermal velocity V_{te1} , the upstream density n_{01} , and the upstream electron plasma frequency ω_{pe1} , respectively.

The actual dispersion relation is solved by assuming that the ions are unmagnetized and the electrons are magnetized as in the previous studies [14, 18]. It should be noted that although both ion and electron components have a certain shift in the v_z space (not shown), the effect of the drift velocity in the z direction is not included in the present analysis.

Figure 5 denotes frequencies (upper panel) and growth rates (lower panel) of the instability-1 ($k > 0$) and instability-2 ($k < 0$) below the electron cyclotron frequency for a variety of wave propagation angles with respect to the ambient magnetic field, θ_{B_k} , as a function of $k_x = k \sin \theta_{B_k}$ and $k_y = k \cos \theta_{B_k}$. For the above parameters, both of the two instabilities are unstable at the phase velocities corresponding to the drift velocities of incoming and reflected ions. In all the runs, obliquely propagating waves with a frequency $\omega < \omega_{ce1}$ are unstable, which corresponds to the MTSI-1 due to incoming ions and the MTSI-2 due to reflected ions. We found that the MTSIs have a maximum growth rate at $k_y l_{i1} \sim 4$. Although the linear growth rates of both MTSI-1 and MTSI-2 are of the same order in the linear analysis, the MTSI-2 is dominant in all the simulation runs. One major reason for this is that the wavenumber resolution in the shock tangential (y) direction is $\Delta k_y = 6.28/l_{i1} \sim 0.25/l_{e1}$ in Run A, $\sim 0.39/l_{e1}$ in Runs B and E, $\sim 0.63/l_{e1}$ in Runs C and F, and $\sim 1.26/l_{e1}$ in Runs D and G, so that the simulation system allows the excitation of waves only with a larger wavenumber ($k_y = k_x / \tan \theta_{B_k} > \Delta k_y$) [18]. The maximum growth rate occurs at $\omega/\omega_{ce1} \sim 0.14$, $k_x l_{e1} \sim 1.26$ in Run A, $\omega/\omega_{ce1} \sim 0.26$, $k_x l_{e1} \sim 1.57$ in Runs B and E, $\omega/\omega_{ce1} \sim 0.47$, $k_x l_{e1} \sim 1.98$ in Runs C and F, which are almost in agreement with the simulation result. For Runs D and G, the system does not have enough frequency and wavenumber resolutions to directly compare the theory and simulation. The result suggests that the MTSI-2 is generated for a wide range of the mass ratio, although the growth rate of the MTSIs becomes smaller as the mass ratio becomes smaller.

Figure 6 denotes frequencies (upper panel) and growth rates (lower panel) of the instability-1 ($k_x > 0$) and the instability-2 ($k_x < 0$) above the electron cyclotron frequency as a function of k_x for Runs C, D, F, and G. For the above parameters, both of the two instabilities are unstable at the phase velocities corresponding to the drift velocities of incoming and reflected ions. In these runs, waves propagating in the direction perpendicular to the shock magnetic field are unstable at $\omega \sim n\omega_{ce1}$, which corresponds to the ECDI-1 due to incoming ions and

TABLE II: Parameters for the Maxwellian velocity distribution functions estimated from Fig.4. The velocity, density and frequency are normalized by the upstream electron thermal velocity V_{te1} , the upstream density n_{01} , and the upstream electron plasma frequency ω_{pe1} , respectively.

Run	V_{di1}	V_{ti1}	n_{i1}	V_{di2}	V_{ti2}	n_{i2}	V_{de}	V_{te}	n_e	ω_{pe}	ω_{ce}
A	0.42	0.06	1.68	-0.32	0.05	1.38	0.08	1.94	3.06	1.75	0.92
B	0.60	0.11	1.68	-0.52	0.07	1.04	0.17	1.76	2.72	1.65	0.92
C	0.96	0.17	1.71	-0.87	0.11	1.27	0.22	1.80	2.98	1.73	0.92
D	2.12	0.28	1.70	-1.85	0.21	1.41	0.32	1.75	3.11	1.76	0.92
E	0.58	0.10	1.72	-0.52	0.06	1.10	0.15	1.89	2.82	1.68	0.59
F	0.99	0.15	1.68	-0.81	0.10	1.37	0.21	1.91	3.05	1.75	0.37
G	2.15	0.30	1.68	-1.42	0.30	1.40	0.56	1.86	3.08	1.75	0.18

the ECDI-2 due to reflected ions. The maximum growth rate of the ECDI-2 occurs at $\omega \sim 3.4\omega_{ce1}$, $k_x l_{e1} \sim -6.3$ in Run D, $\omega \sim 3.1\omega_{ce1}$, $k_x l_{e1} \sim -12.5$ in Run F, and $\omega \sim 3.2\omega_{ce1}$, $k_x l_{e1} \sim -8.7$ in Run G, which are almost in agreement with the simulation result. In Run C, on the other hand, the maximum growth rate of the ECDI-2 occurs at $\omega \sim 3.1\omega_{ce1}$, $k_x l_{e1} \sim -10.6$ in the linear analysis, while there is no wave excitation by ECDI-2 in the simulation. This is because Run C does not have enough resolution for waves at $k_x = 10/l_{e1} = 1/\lambda_{De1}$. We performed a high-resolution ($\Delta x = 0.1\lambda_{De1}$) 1D simulation, and confirmed that the ECDI-2 is weakly generated. It should be noted that the linear analysis for Runs A, B and E shows a positive but small ($\gamma/\omega_{ce1} < 5$) growth rate for the ECDIs at a wavelength shorter than the electron Debye length ($k_x \lambda_{De1} > 1$). However, full particle simulations do not show the generation of the ECDIs even with a higher resolution.

Although both ECDI-1 and ECDI-2 have a positive growth rate in the linear analysis, the ECDI-1 is not generated in these simulation runs. Note that the simulation system has enough spatial resolution for ECDI-1 in Runs D, F and G (see Table 1). Here we present several reasons for this by using the temporal development of the foot region shown in Fig.7. First, we analyze the velocity distribution functions near the ramp-side of the foot region, while the ECDI-1 is generated from the upstream-side of the foot region. Second, waves excited in the ramp-side of the foot region quickly reach the shock front and the ECDI-1 does not have enough growth time. Third, the relative drift between the incoming ions and electrons arises later in the broadening phase. The incoming ions move through a distance of $2.4l_{i1}$ in a time of $0.4/\omega_{ci1}$ (because of $M_A = 6$). As seen in Fig.7, the structure of the foot region quickly changes on the timescale of $0.1/\omega_{ci1}$, and the relative drift between the incoming ions and electrons exists in a narrow region of $< 2l_{i1}$.

IV. CONCLUSION AND DISCUSSION

The present 2D full particle simulations suggested that the ion-to-electron mass ratio affects microinstabilities in the foot region of perpendicular collisionless shocks. Both simulation result and linear analysis clearly show that

electromagnetic oblique whistler waves due to the MTSI are dominant with a large mass ratio, while electrostatic ECH waves due to the ECDI are dominant with a small mass ratio.

The electrostatic ECH waves contribute to the generation of nonthermal population of electrons [22]. The electromagnetic oblique whistler waves contribute to the electron heating in the direction parallel to magnetic fields, which slightly modifies the shock jump condition. The influence of the excited waves to ion heating is small in the present study.

It should be noted that the MTSIs are generated even with small mass ratios (Runs B-G), which is seemingly inconsistent with the previous expectation [14]. However, the previous linear analysis by Matsukiyo and Scholer [14] was done by using local (foot) plasma parameters as normalization factors, although the linear analysis here utilizes the upstream plasma parameters as normalization factors. The period of reformation is of the order of upstream ion gyro period which is often about three times longer than a local ion gyro period estimated by using the local magnetic field value in the foot.

In most of the cases ($m_i/m_e \geq 100$: except for Runs D and G), the MTSIs are predominant in terms of wave power compared with the ECDIs. As pointed out in the previous studies [31, 32], ECDI saturates at a low level. Furthermore, it is confirmed in a two dimensional periodic (local) simulation that the MTSI finally survives even though the ECDI has a larger growth rate [16] if MTSI and ECDI are simultaneously present. Here, we confirmed such properties in our self-consistent 2D shock simulations.

In the shock-tangential direction, large-amplitude fluctuations on the ion inertial scale are commonly exist at the shock front, which are known as the “ripples” [33]. Recent full particle simulations with a large system size suggested that shock-front ripples change the structure of shocks and enhance microinstabilities at the shock front [18, 22, 29, 30]. In the present study, however, the generation of the ripples is not included because the system length in the shock-tangential direction is too short. The present linear analysis shows that the MTSIs have the maximum growth rate at $k_{\parallel} l_{i1} \sim 4$, which suggests that the oblique whistler waves can couple with L-mode ion-cyclotron waves at the shock overshoot that are a seed

perturbation of the ripples. A large-scale 2D simulation including shock-front ripples is currently undertaken to understand the competition between the ripples and microinstabilities, and is reported in a future paper.

Acknowledgments

This work was supported by MEXT/JSPS under Grant-in-Aid for Scientific Research on Innovative Ar-

eas No.21200050 and Grant-in-Aid for Young Scientists (B) No.22740323 (S. M.) and No.21740184 (R. Y.). The computer simulations were performed on the DELL PowerEdge R815 supercomputer system at the Solar-Terrestrial Environment Laboratory (STEL) and the Fujitsu FX1 and HX600 supercomputer systems at the Information Technology Center (ITC), Nagoya University, as HPC joint research programs at STEL, ITC, and Joint Usage/Research Center for Interdisciplinary Large-scale Information Infrastructures (JHPCN).

-
- [1] D. Biskamp and H. Welter, *Nuclear Fusion* **12**, 663 (1972).
 - [2] O. Buneman, *Phys. Rev. Lett.* **1**, 8 (1958).
 - [3] H. V. Wong, *Phys. Fluids* **13**, 757 (1970).
 - [4] D. W. Forslund, R. L. Morse, and C. W. Nielson, *Phys. Rev. Lett.* **25**, 1266 (1970).
 - [5] N. Shimada and M. Hoshino, *Astrophys. J.* **543**, L67 (2000).
 - [6] L. Muschietti and B. Lembège, *Adv. Space Res.* **37**, 483 (2006).
 - [7] N. A. Krall and P. C. Liewer, *Phys. Rev. A* **4**, 2094 (1971).
 - [8] C. N. Lashmore-Davies, *Phys. Fluids* **14**, 1481 (1971).
 - [9] E. Ott, J. B. McBride, J. H. Orens, and J. P. Boris, *Phys. Rev. Lett.* **28**, 88 (1972).
 - [10] J. B. McBride and E. Ott, *Phys. Lett.* **39A**, 363 (1972).
 - [11] J. B. McBride, E. Ott, J. P. Boris, and J. H. Orens, *Phys. Fluids* **15**, 2367 (1972).
 - [12] C. S. Wu, Y. M. Zhou, S. T. Tsai, S. C. Guo, D. Winske, and K. Papadopoulos, *Phys. Fluids* **26**, 1259 (1983).
 - [13] M. Scholer, I. Shinohara, and S. Matsukiyo, *J. Geophys. Res.* **108**, 1014 (2003).
 - [14] S. Matsukiyo and M. Scholer, *J. Geophys. Res.* **108**, 1459 (2003).
 - [15] M. Scholer and S. Matsukiyo, *Ann. Geophys.* **22**, 2345 (2004).
 - [16] S. Matsukiyo and M. Scholer, *J. Geophys. Res.* **111**, A06104 (2006).
 - [17] S. Matsukiyo, *Phys. Plasmas* **17**, 042901 (2010).
 - [18] T. Umeda, Y. Kidani, S. Matsukiyo, and R. Yamazaki, Modified two-stream instability at perpendicular collisionless shocks: Full particle simulations, *J. Geophys. Res.* **117**, A03206 (2012).
 - [19] T. Umeda, Y. Omura, T. Tominaga, and H. Matsumoto, *Comput. Phys. Commun.* **156**, 73 (2003).
 - [20] T. Umeda and R. Yamazaki, *Earth Planets Space* **58**, e41 (2006).
 - [21] T. Umeda, M. Yamao, and R. Yamazaki, *Astrophys. J.* **681**, L85 (2008).
 - [22] T. Umeda, M. Yamao, and R. Yamazaki, *Astrophys. J.* **695**, 574 (2009).
 - [23] M. M. Leroy, C. C. Goodrich, D. Winske, C. S. Wu, and K. Papadopoulos, *Geophys. Res. Lett.* **8**, 1269 (1981).
 - [24] M. M. Leroy, D. Winske, C. C. Goodrich, C. S. Wu, and K. Papadopoulos, *J. Geophys. Res.* **87**, 5081 (1982).
 - [25] T. Umeda, Y. Omura, and H. Matsumoto, *Comput. Phys. Commun.* **137**, 286 (2001).
 - [26] P. D. Hudson, *Planet. Space Sci.* **18**, 1611 (1970).
 - [27] K. B. Quest, *Phys. Rev. Lett.* **54**, 1872 (1985).
 - [28] B. Lembège and J. M. Dawson, *Phys. Fluids* **30**, 1767 (1987).
 - [29] T. Umeda, Y. Kidani, M. Yamao, S. Matsukiyo, and R. Yamazaki, *J. Geophys. Res.* **115**, A10250 (2010).
 - [30] T. Umeda, M. Yamao, and R. Yamazaki, *Planet. Space Sci.* **59**, 449 (2011).
 - [31] M. Lampe, W. M. Manheimer, J. B. McBride, J. H. Orens, K. Papadopoulos, R. Shanny, and R. N. Sudan, *Phys. Fluids* **15**, 662 (1972).
 - [32] C. S. Wu, D. Winske, Y. M. Zhou, S. T. Tsai, P. Rodriguez, M. Tanaka, K. Papadopoulos, K. Akimoto, C. S. Lin, M. M. Leroy, and C. C. Goodrich, *Space Sci. Rev.* **37**, 63 (1984).
 - [33] D. Winske and K. B. Quest, *J. Geophys. Res.* **93**, 9681 (1988).

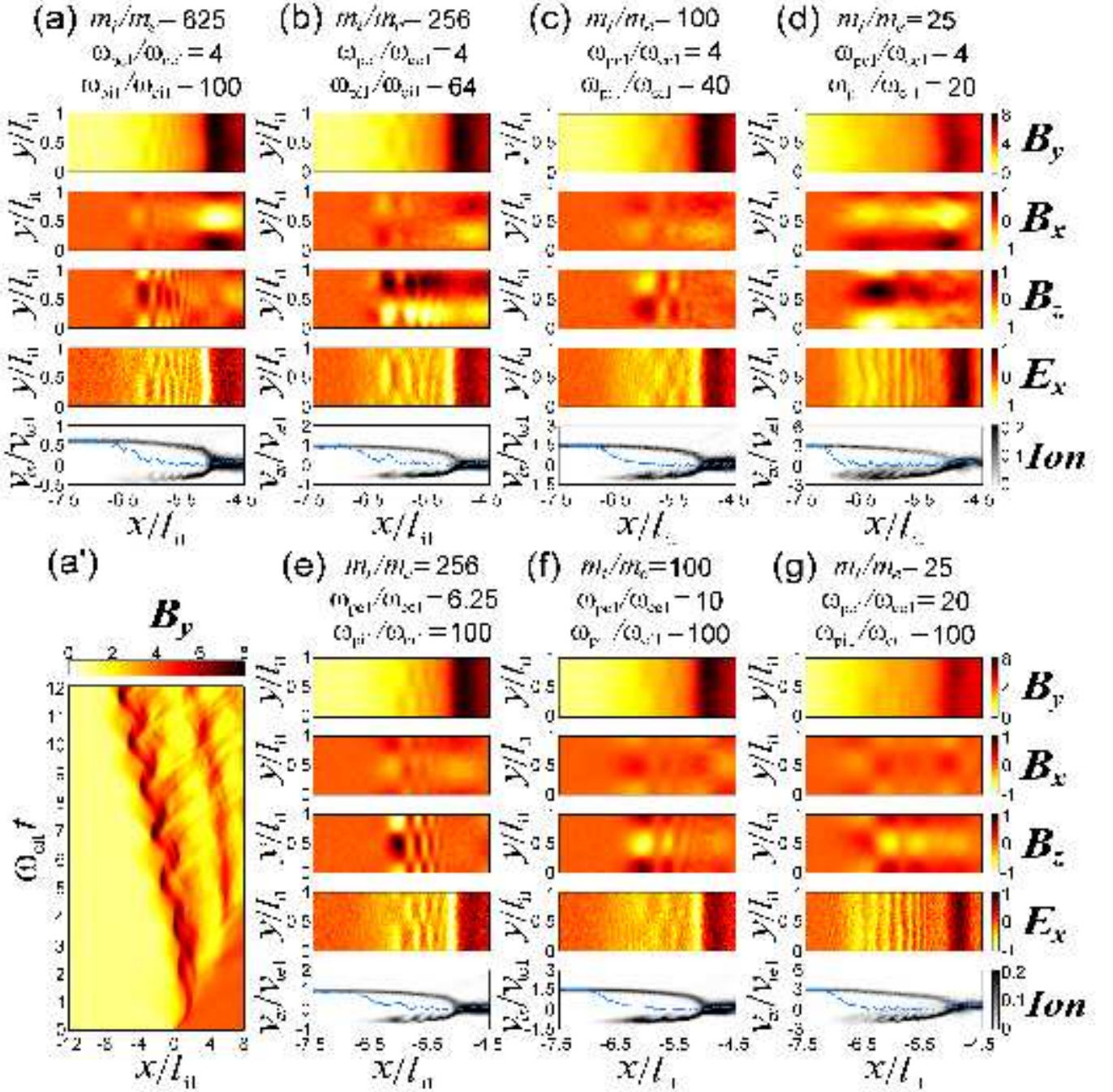


FIG. 1: The evolution of the perpendicular shock in Runs A-G. (a-g) Magnetic field B_x , B_y , B_z components, electric field E_x component, and corresponding $x - v_x$ phase-space distribution function of ions at $\omega_{ci1}t = 10.2$ in Runs A-G. The solid line in the phase-space plot indicates the electron bulk velocity. (a') Tangential magnetic field B_y averaged over y as a function of position x and time t in Run A. The position and time are normalized by l_{i1} and $1/\omega_{ci1}$, respectively. The magnitude of magnetic field is normalized by the initial upstream magnetic field B_{y01} . The magnitude of electric field is normalized by the motional electric field E_{z0} .

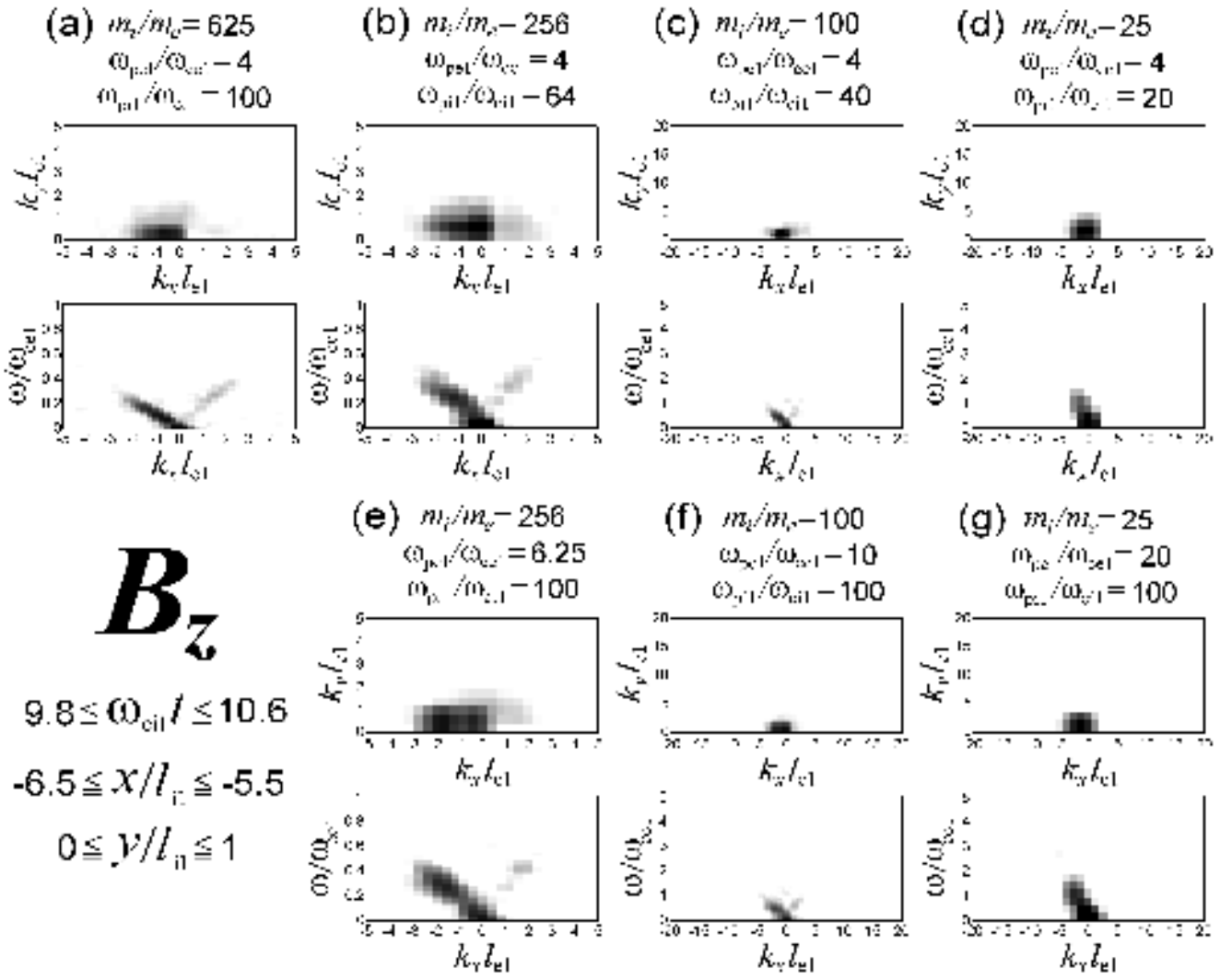


FIG. 2: Spectra of B_z component for Runs A-G. The magnitude is plotted in a logarithmic scale from $10^{-3}B_{y01}$ to $10^{-1}B_{y01}$.

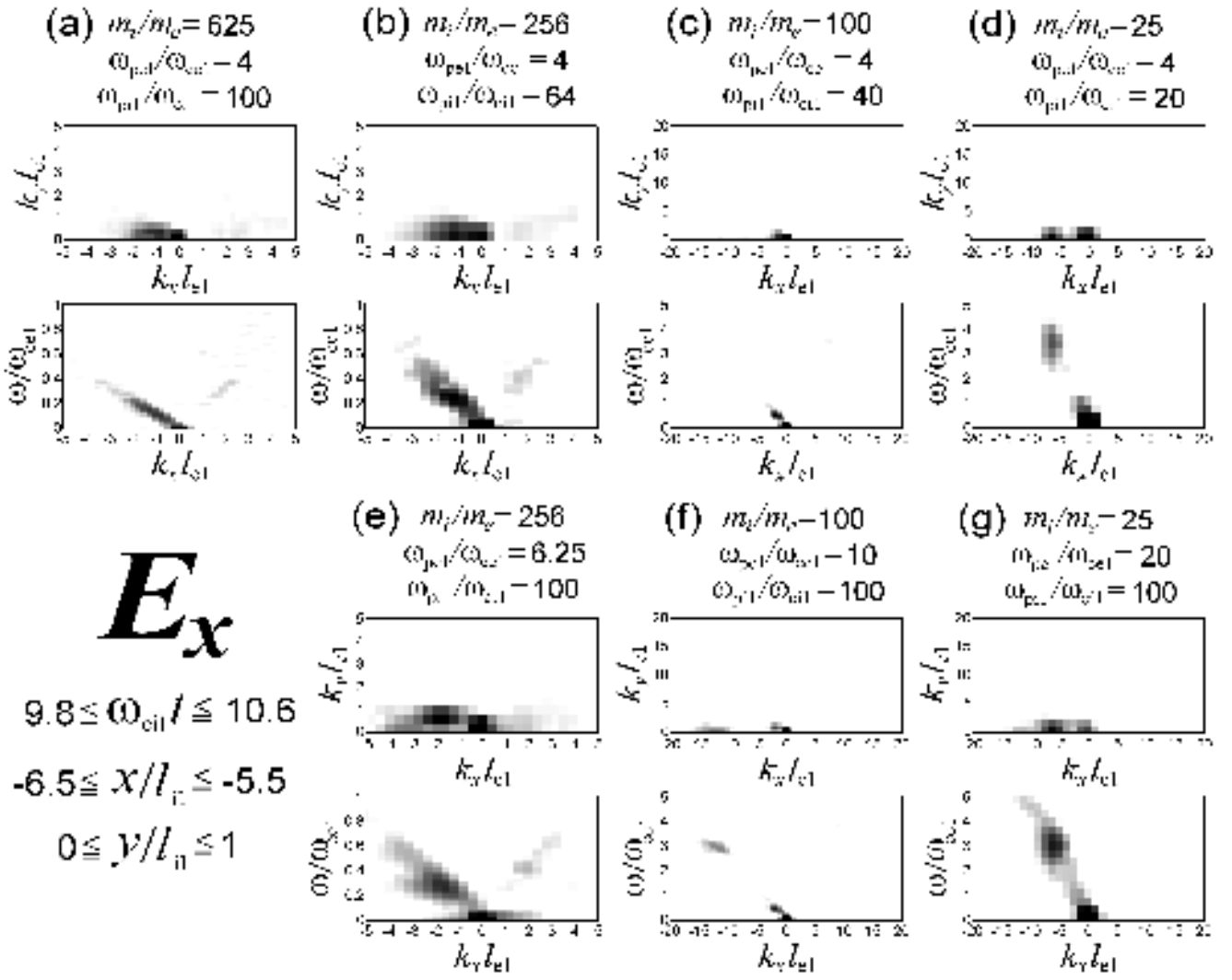


FIG. 3: Spectra of E_x component for Runs A-G with the same format as Fig.2. The magnitude is plotted in a logarithmic scale from $10^{-3}E_{z0}$ to $10^{-1}E_{z0}$.

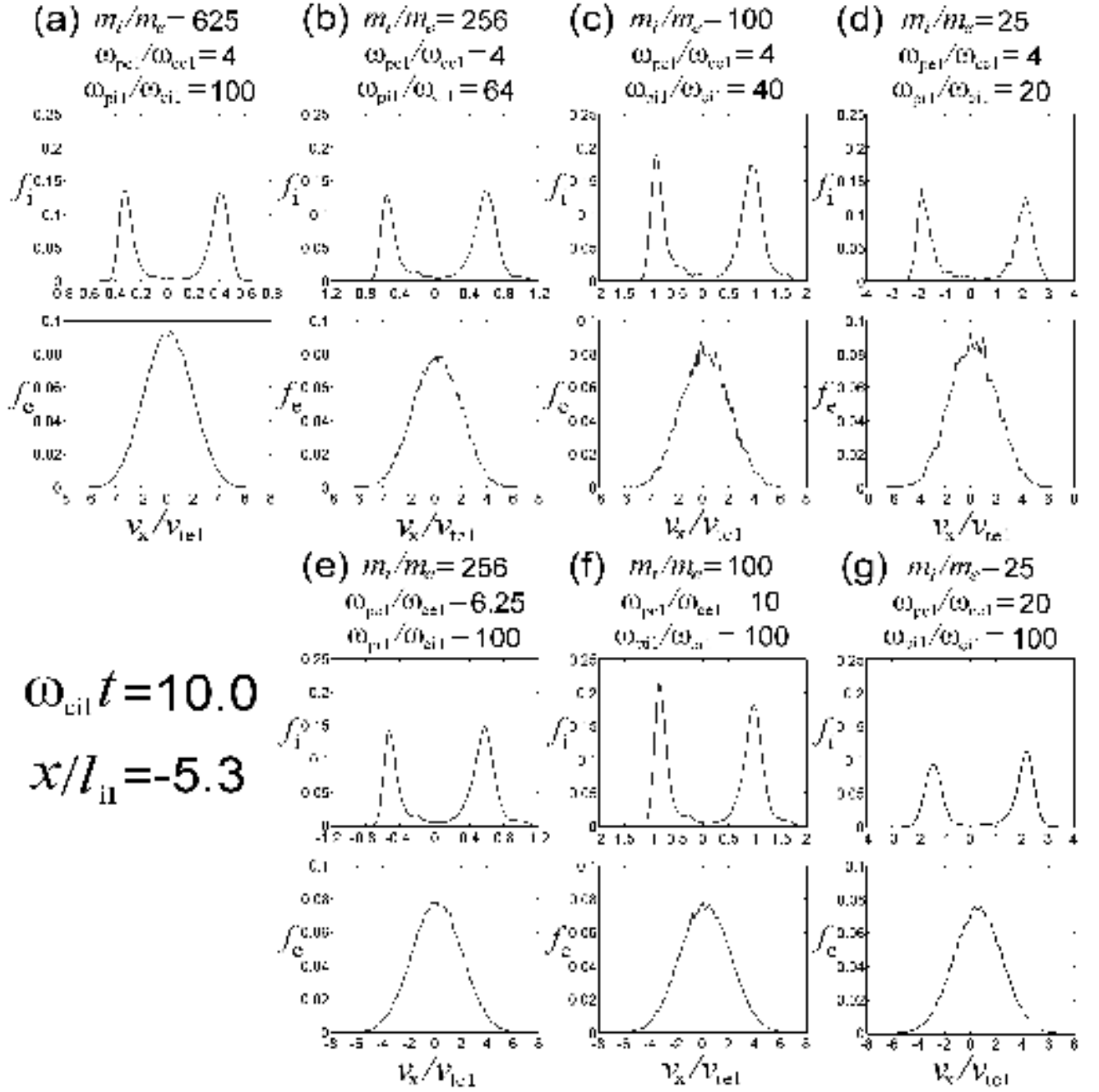


FIG. 4: Reduced velocity distribution functions of ions and electrons ($f_i(v_x)$ and $f_e(v_x)$) averaged over y at the shock foot just before the generation of instabilities in Runs A-G.

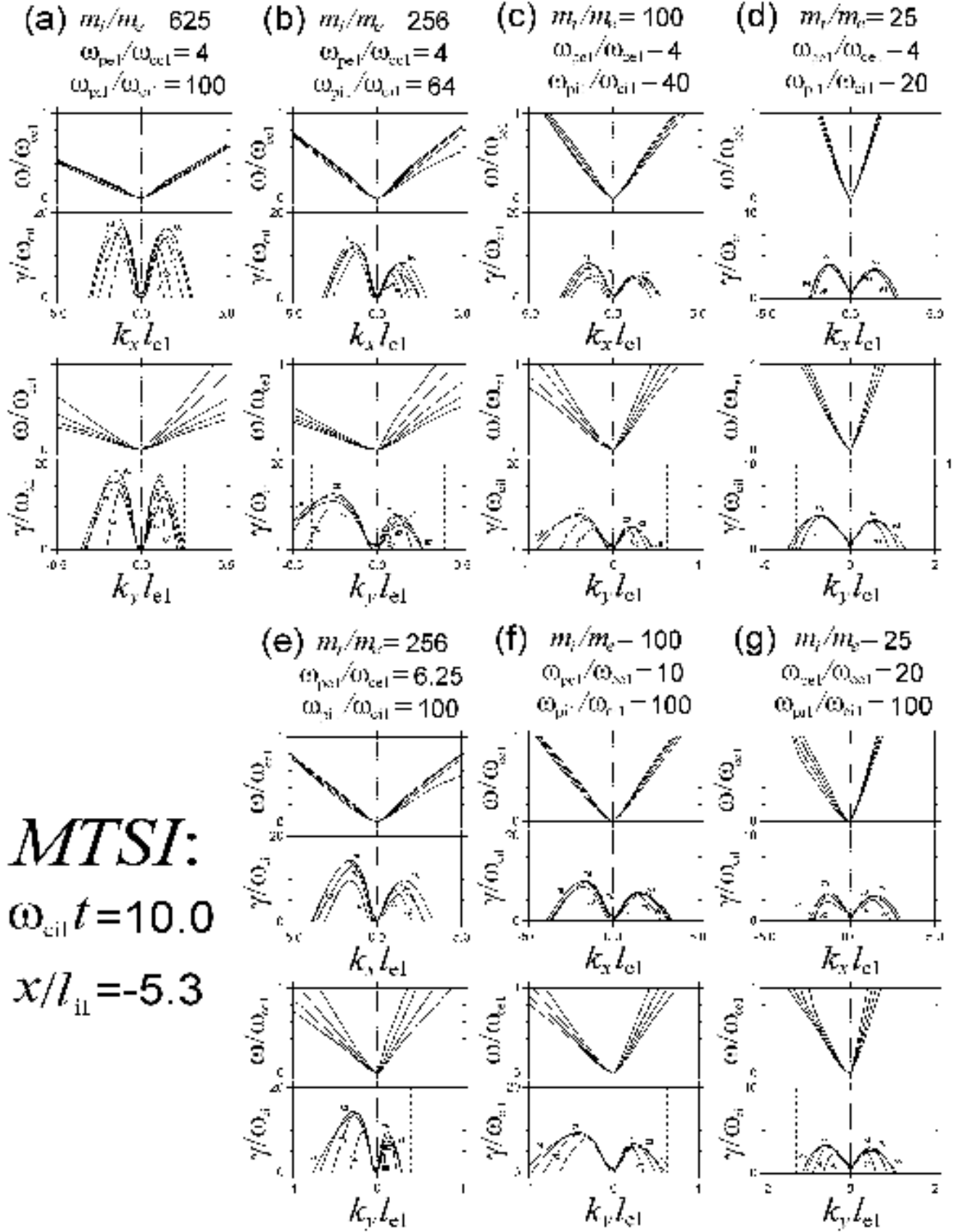


FIG. 5: Linear dispersion relations of the MTSI-1 ($k_x > 0$) and MTSI-2 ($k_x < 0$) for Runs A-G based on the velocity distribution functions in Fig.4. Frequencies and growth rates are plotted for a variety of wave propagation angles with respect to the ambient magnetic field, θ_{B_k} , as a function of $k_x = k \sin \theta_{B_k}$ and $k_y = k \cos \theta_{B_k}$.

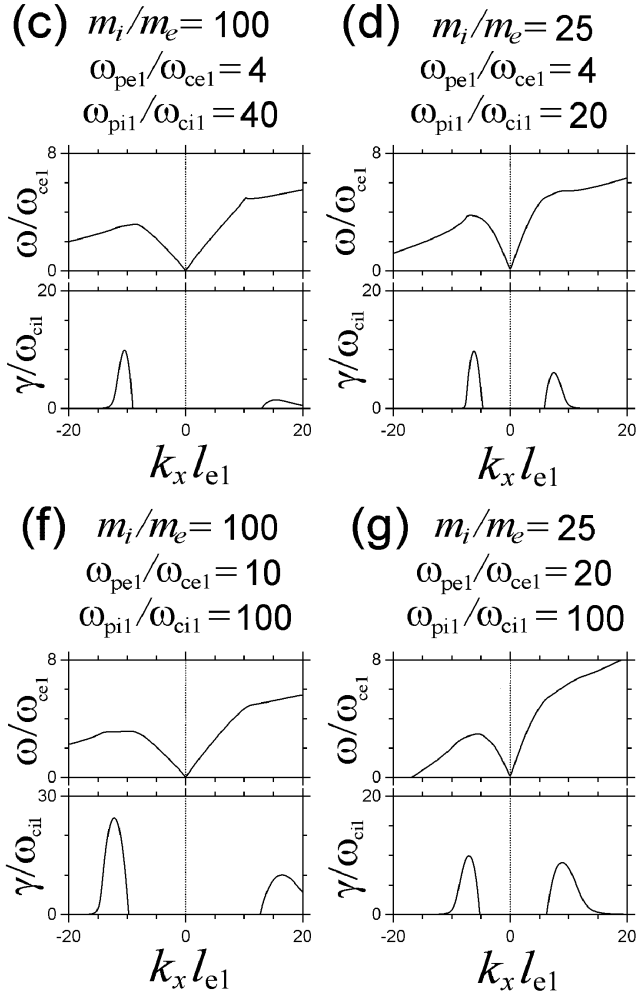


FIG. 6: Linear dispersion relations of the ECDI-1 ($k_x > 0$) and ECDI-2 ($k_x < 0$) for Runs C, D, F and G based on the velocity distribution functions in Fig.4.

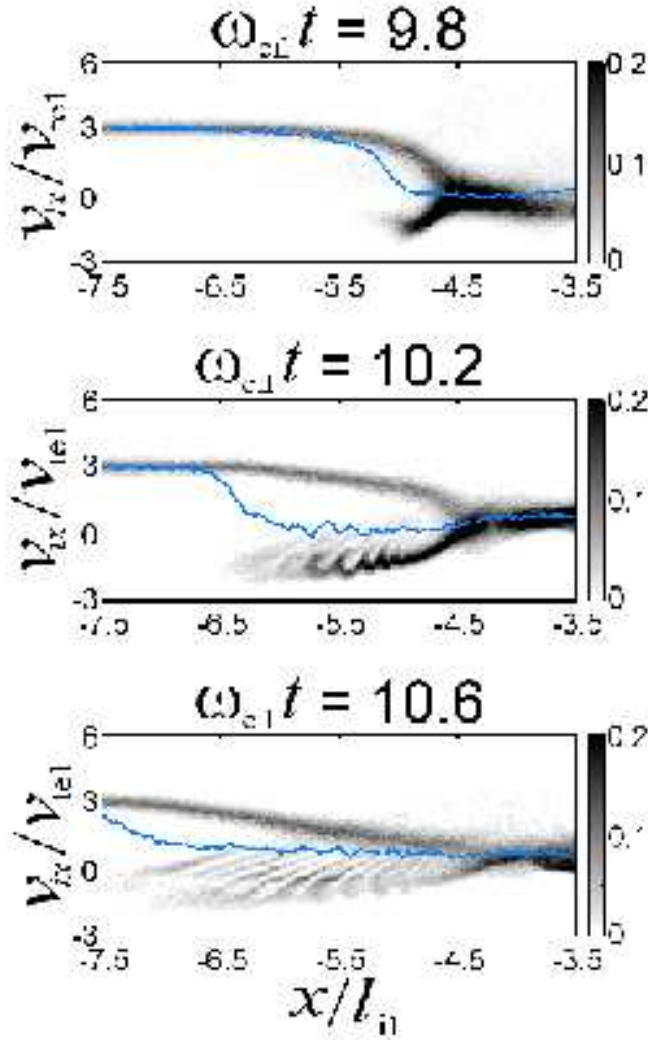


FIG. 7: The $x - v_x$ phase-space distribution function of ions at different times in Run G. The solid line in the phase-space plot indicates the electron bulk velocity.